Available online at www.sciencedirect.com
SCIENCE DIRECT®
International Journal of Heat and Mass Transfer 48 (2005) 4316–4332
International Journal of HEAT and MASS TRANSFER
www.elsevier.com/locate/ijhmt

Microscale heterogeneous boiling on smooth surfaces—from bubble nucleation to bubble dynamics

J. Li, G.P. Peterson *

Department of Mechanical, Aerospace and Nuclear Engineering, Rensselaer Polytechnic Institute, 110 8th Street, Troy, NY 12180, United States

Received 18 October 2004; received in revised form 27 May 2005
Available online 28 July 2005

Abstract

In this investigation, boiling incipience and bubble dynamics on a microheater with a geometry of 100 μm × 100 μm fabricated with MEMS technology are evaluated using a high-speed digital camera. For the purpose of comparison with conventional boiling heat transfer, boiling incipience and bubble dynamics are also studied on a carefully selected microheater with a fabricated defect (i.e., a microcavity on the heater surface). Of industrial interest are the effects of dissolved gases on boiling incipience and bubble dynamics, which are also discussed in detail. The possible nucleation temperature (or incipience temperature) is analyzed and discussed from the perspective of the measured bulk temperature of the microheater and a 3D heat conduction numerical model. The time-resolved bubble dynamics (i.e., the bubble size evolution, interface velocity and interface acceleration) are all presented along with high-speed digital images. Based upon this investigation, it is clear that explosive boiling can take place on a smooth surface no matter how slow the heating rate, and dissolved gases have a significant influence on the incipience temperature and bubble behavior. Furthermore, this study illustrates that the classical kinetics of boiling can explain the explosive boiling occurring on a smooth surface in principle and can provide a useful guide for the design of microscale heat transfer and/or MEMS devices. Although unexpected, due to the gravitational effects, Marangoni flow on the vapor–liquid interface induced by the temperature gradient was also observed.

Keywords: Bubble nucleation; Bubble dynamics; Boiling incipience; Microheater; Marangoni flow

1. Introduction

Due to continued developments in the microelectronics industry during the last decade there has been a growing interest in liquid–vapor phase-change heat transfer at the microscale. This increased interest is in part driven by increases in the packaging density of components, which results in significantly higher heat fluxes. As the air cooling limit is reached, liquid cooling, with or without phase change, is the first alternative. Two ranges of heat flux can be loosely identified relative to the magnitude of this heat dissipation: the high-flux range, with cooling heat flux requirements on the order of 10^2–10^3 W/cm^2, and the ultra-high heat flux range, with heat fluxes above 10^3 W/cm^2 [1]. The high-flux range is

* Corresponding author. Tel.: +1 518 276 6487; fax: +1 518 276 4061.
E-mail address: peterson@rpi.edu (G.P. Peterson).

0017-9310/$ - see front matter © 2005 Elsevier Ltd. All rights reserved.
doi:10.1016/j.ijheatmasstransfer.2005.05.022

Nomenclature

C_P	specific heat of platinum
e_R	electrical Resistivity
I	current
$\dot{Q}$	inner heat resource; power
r	bubble radius
$\dot{r}$	bubble interface velocity
$\ddot{r}$	bubble interface acceleration
r_0	initial radius of bubble
R	resistance
t	time
T	temperature
TCR	thermal coefficient of resistivity
ΔV	voltage drop

Greek symbols

α	natural convection heat transfer coefficient
ε	emissivity
λ	thermal conductivity
ρ	density of platinum

Subscripts

Au	gold
PR	precision resistors
Pt	platinum

presently encountered in high-performance supercomputers, advanced military avionics and similar high performance devices and systems. The ultra-high heat flux range is typically encountered in fusion reactors, high-efficiency (continuous-wave) short-pulse lasers and X-ray synchrotrons, etc. Liquid cooling can be employed with or without boiling as a potential approach to solving the problems associated with these devices, and has been the subject of numerous studies in recent years. A second reason for the growing interest in liquid–vapor phase-change heat transfer at the microscale, is that bubble actuation at the microscale under pulsed heating has been used successfully in thermal ink jet printers. A number of other novel applications utilizing microscale bubble actuation are currently being explored, e.g., bubble actuated pumps [2], bubble-actuated micro-mixers [3] and bio-sensors [4].

It is well known that boiling requires that the temperature of the heated device exceed the saturation temperature of the pure liquid. The liquid adjacent to the device surface must first be superheated by a few degrees above the saturation temperature in order to form the first bubble. One of the key concerns in the implementation of phase-change cooling schemes using dielectric coolants is the uncertainty surrounding the initiation of nucleate boiling. In these applications, boiling incipience often occurs at temperatures much higher than expected. This excess superheat may be dissipated quickly by vigorous boiling, but may also result in damage to the device due to thermal shock [1]. Unsteady-state phase change under pulsed heating is much more closely related to bubble nucleation and a clear understanding of the nucleation temperature and bubble behavior is important in the future development of MEMS technology.

The optimal boiling incipience temperature for different situations is still unknown because so little is known and there is so much variation in the data reported in the published literature, especially when the influence of micro-cavities and dissolved gases are factored into the determination of the incipience and/or nucleation temperatures. Classical theory has already revealed some of the mechanisms involved in the boiling process.

Hsu [5] has proposed a criterion for bubble survival in pool boiling and successfully demonstrated that this criterion can predict, quite accurately, the boiling incipience temperature and the corresponding heat flux. However, this theory is suitable only for cavities ranging in size from 10 to 1000 μm. A classical *kinetics of boiling* approach can be used to explain the physics behind homogeneous and heterogeneous nucleation occurring in pool boiling, but the experimental data are often far below the values predicted by the kinetics of boiling. For example, Cole [6] has analyzed and summarized in detail the physical mechanisms for bubble nucleation at very small length scales, which yields a homogeneous nucleation temperature of approximately 180 K above the saturation temperature for water at atmospheric pressure. Until recently, only rapid transient nucleate boiling under pulsed heating [7–12] has demonstrated that homogenous or heterogeneous nucleation plays a defining role in the boiling process and little evidence exists that the temperature of boiling incipience will approach the value predicted by the kinetics of boiling. Even so, there still exists a significant difference among these experimental data [7–12]. It is important to understand that the kinetics of boiling can help to explain not only the transient boiling process, but also the boiling modes at the microscale, e.g., the quasi steady-state boiling processes observed at the microscale. Unfortunately, there is little evidence to validate the accuracy of the kinetics for quasi steady-state conditions.

Recently, a series of experiments was conducted to examine and understand nucleate boiling on a

microscale heater in which the heater temperature was maintained at a constant value [13–15]. Chen et al. [14] found that when the superheat approached the homogeneous nucleation temperature, the vapor immediately expanded and was distributed over an area well beyond the heater surface area, but when the superheat of the heater was less than the homogeneous nucleation temperature, the bubble formation was always initiated with nucleation of small bubbles and their coalescence. Unfortunately, even though a high-speed camera was used, information on the initial stage of bubble formation was not presented and thus it is very hard to determine if this microscale boiling has a definitive connection to the kinetics of boiling.

The bubble dynamics of a boiling system from nucleation in the liquid to the detachment from the heated surface is not clearly understood. The Rayleigh–Plesset equation can be used to describe the bubble growth in general, however, the initial nonequilibrium vapor pressure is not clearly understood. Currently, there exists a number of models [16–19], some of which yield reasonable agreement with the experimental data, if some important assumptions are made, e.g., the assumption of the inner bubble thermodynamic parameters (temperature or pressure). General agreement exists that bubble growth includes two stages: the dynamic stage and the heat transfer stage. However, how to identify or distinguish between these two stages is unclear due to the questions surrounding the nonequilibrium vapor pressure [20].

In the current investigation, a microscale platinum heater with a very smooth surface (average roughness of 50 Å) was fabricated on a Pyrex wafer. The *lowest* nucleation temperature in water, with or without dissolved gas, was identified by carefully controlling the power input. Quasi steady-state and transient boiling under pulsed heating were explored and both bubble nucleation and bubble growth were observed using a high-speed digital camera. For the first time, explosive boiling phenomena were observed over the entire range, including quasi steady-state boiling, and the boiling incipience temperature was analyzed. Comparisons of the bubble behavior in a microcavity, with the time-resolved bubble dynamics associated with explosive boiling on a smooth surface indicated that the resulting phenomena were much different from conventional bubble dynamics. These unique bubble nucleation and growth phenomena are reported here for the first time and reveal considerable insight into the boiling mechanism occurring in MEMS applications.

2. Experimental system

The microheater used in the current experimental investigation is shown in Fig. 1(a). The microheater

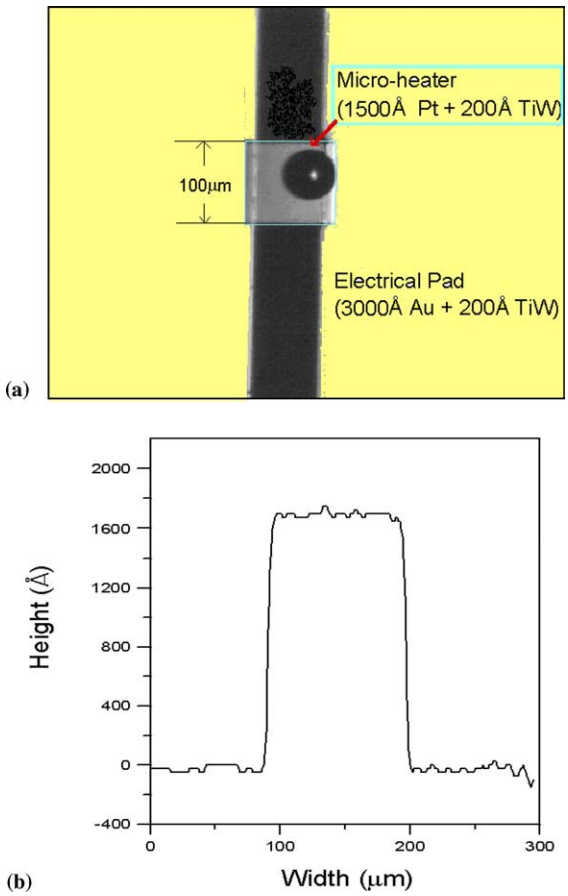

Fig. 1. The fabricated microheater: (a) Photo of the microheater and the electrical pad and (b) surface roughness of the microheater.

was created using microfabrication technology and a lift-off metallization technique. A 200 Å TiW film (for adhesion) and 1500 Å platinum film were sputtered on a Pyrex wafer coated with a photoresist, after patterning with photolithography. Following a lift-off process in acetone, the process was repeated for a gold pad with a thickness of 3000 Å of Au and 200 Å of TiW. The length and width of the gold pad were 10 mm and 2 mm, respectively. The width and length of the platinum heater were both 100 μm. It should be noted that there was an overlap of the gold pad, of 10 μm on both sides, used for the necessary connections, so that the actual width of the heater was 80 μm. The surface roughness of the microheater was measured using a scanning profilometer and is given in Fig. 1(b). The average roughness of the microheater surface is approximately 50 Å (5 nm). This roughness is in the range of the critical bubble size for homogeneous bubble nucleation, thus, avoiding the influence of cavity size on bubble nucleation.

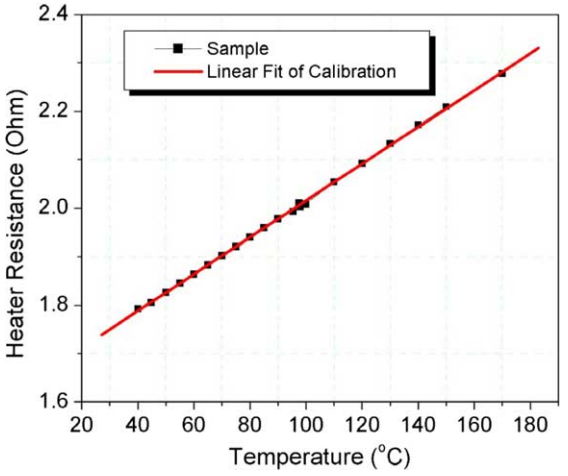

Fig. 2. The calibration of the microheater specimen.

The results of the calibration of the temperature and the resistance of the microheater are shown in Fig. 2. The dark squares shown are the calibration results achieved by placing the microheater in a thermal bath and/or on a hot plate and isolating it with a cover on top of the microheater, in order to suppress the temperature oscillations. Two microscale T-type thermocouples were attached to the Pyrex wafer very close to the microheater to record the temperature variation using a digital thermometer (Omega HH23 microprocessor thermometer). After several heating and cooling cycles in the thermal bath, the response of the microheater resistance with the temperature variation was transferred to a digital data acquisition system (HP 3478A Multimeter) and recorded. A linear fit was applied to the calibration data, resulting in a gradient of 0.00379 Ω/°C as shown in Fig. 2. It should be noted here that this resistance calibration considers all of the resistances of the microheater, i.e., the TiW, gold pad and the electrical wire soldered to the gold pad for circuit connections. For ambient conditions, the total resistance of the gold pad and electrical wires was approximately 1.0788 Ω as measured by a digital multimeter at room temperature.

The experimental test facility is illustrated in Fig. 3(a), and includes a heating unit, a control unit, a data acquisition system and the experimental test section. The heating unit was a DC power supply and an electronic circuit through which the pulse magnitude or the total voltage input could be adjusted. The data acquisition unit included a digital oscilloscope (Tektronix TD2014) with a sampling rate of 1.0 GS/s or higher, which was used to record the voltage drop on different resistance elements. A microscope (500X, Olympus BXFMF) and a digital high-speed camera (Redlake MotionScope PCI 2000S) with a maximum recording rate of 2000 fps was used to record bubble formation and behavior. The control unit consisted of the required control and trigger generators. The voltage pulse was used as the prime trigger for the pulsed heating and the quasi steady-state process, respectively. The imaging card connected to a CCD camera and the digital oscilloscope were triggered at the same time. In this way, all of the data acquisition equipment was synchronized. The test section included a Pyrex Petri dish which served as a water vessel and a die-sized Pyrex wafer with the microheater fabricated on the surface. The main resistance elements in the circuit were the precision resistors (PR) and the microheater specimen. These resistance elements were subjected to a continuous electric power directly from DC power supply or a periodic electric pulse from a waveform generator and an amplifier circuit (which was integrated on the control board). The precision resistors were used for current measurement, $I(t) = \Delta V_{PR}(t)/R_{PR}$ and the configuration of the voltage drop measurement on these resistance elements is shown in Fig. 3(b). The tips of the measuring probe connected to the digital oscilloscope were attached very close to the pin of the resistors and the microheater, in order to avoid the introduction of errors due to the connecting wires.

As shown in Fig. 4, which illustrates the calibration of the precision resistors, during a 140 ms electric pulse, the resistance of the precision resistors does not change. From the manufacture data sheets, the temperature coefficient (TCR) of these devices was ±20 ppm/°C and if compared to the TCR of standard platinum (3850 ppm/°C), the variation of the resistance during electrical heating was negligible.

Because the properties of water are well known and can easily be found in the literature (e.g., air solubility in water), this experimental investigation utilized pure, deionized water as the working fluid. The bulk fluid temperature was approximately 25 °C for un-degassed water and 40 °C for degassed water in order to avoid evaporation of the liquid and blurring of the objective lens of the microscope (The ambient pressure was 1 atm and, therefore, there was a subcooling of about 75 and 60 °C respectively.) The liquid was maintained at 5 mm above the microheater to avoid the influence of the surface on the bubble behavior, as in pool boiling. For quasi steady-state boiling, a slow, but steadily increasing rate of 0.1 V/s of overall voltage input was applied to the circuit. After initial bubble formation, the total voltage input was held constant to explore the bubble behavior. For the transient boiling study, a series of voltage pulses with 120 ms duration were conducted with increases of 0.1 V in amplitude. In order to determine the effects of dissolved gas on boiling incipience and bubble dynamics, two different cases were evaluated: one with gas dissolved in twice-distilled water, and the other with twice-distilled water from which the dissolved gas was removed by boiling the water for more than 30 min in the Pyrex Petri dish.

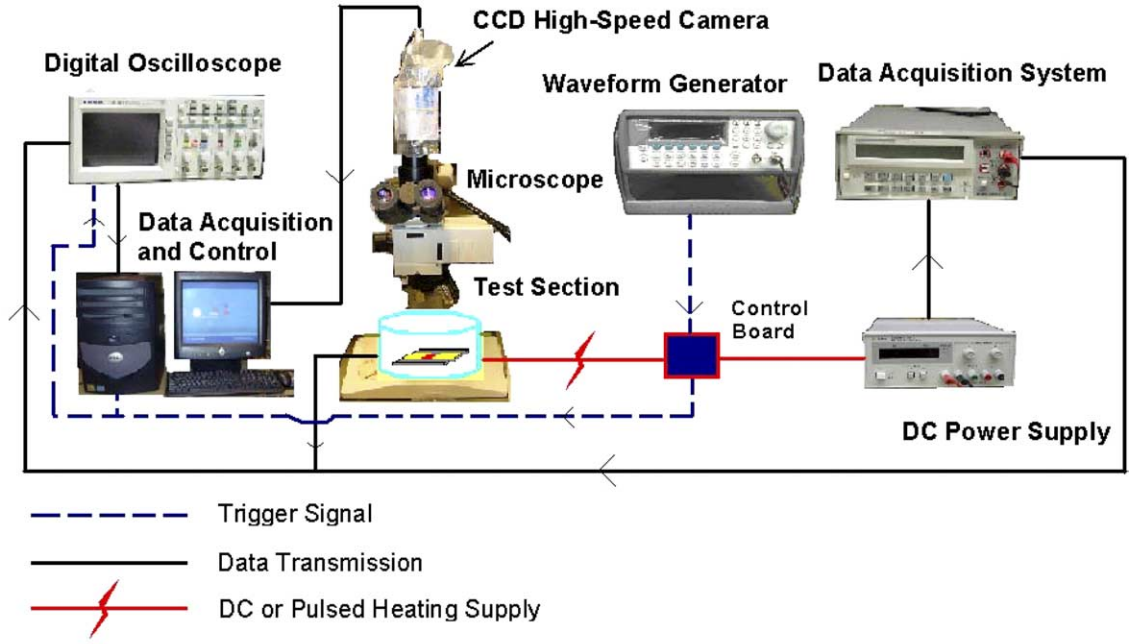

(a)

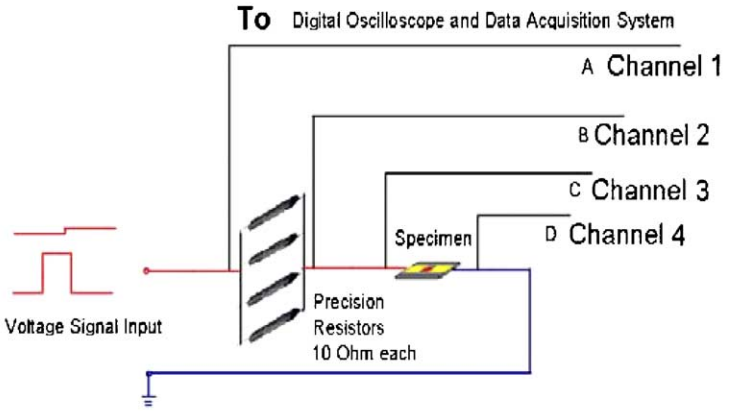

(b)

Fig. 3. The experimental setup and the resistance measurement circuit: (a) Experimental setup and (b) resistance measurement circuit.

The primary sources of uncertainty in the present experiments as presented in the following sections, are the ambient noise and the residual thermal stress of the microheater, due to the microfabrication. These two unknown factors had a negative influence on the accuracy of the measurements, but their impact on the magnitude of the measured values was determined to not be significant. The difference between the two thermocouples attached to the microheater specimen used for calibration was less than 0.1 °C and the value as measured by a digital multimeter was unchanged to four significant digits during calibration. Other resistance elements were all measured with a digital multimeter to the same level of accuracy. During the experiments, the uncertainty of the temperature measurement was determined by repeating experiments to be less than ±6% (or ±5 °C for a measured value of 85 °C, ±10 °C for a measured value of 180 °C). If the nonuniformity of the temperature distribution as revealed by a detailed 3D numerical simulation is taken into consideration, the

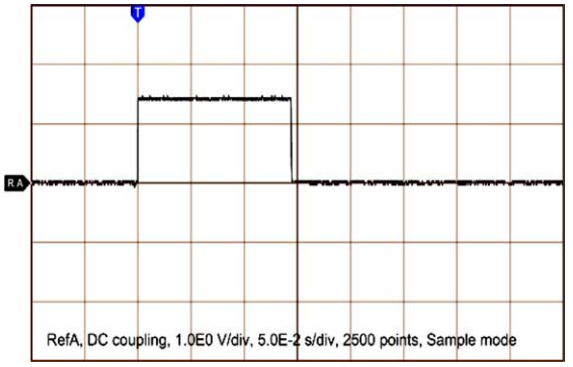

Fig. 4. Calibration of precision resistors.

overall uncertainty for the measured boiling incipience temperature will be less than ±15% (or ±10 °C for a measured value of 85 °C and ±25 °C for a measured value of 180 °C).

3. Data reduction

The temperature of the heater was determined from the relationship between the temperature and the resistance of the microheater. The resistance of the microheater varied almost linearly as the ambient temperature changed. With the calibration results shown in Fig. 2 and the curve fit, the resistance of the microheater, R_{heater}, could be related to the temperature as

$$R_{heater}(T_{heater}) = R_0 \cdot f(R_{heater}(t)) = R_0(1 + \theta \cdot T_{heater,bulk}) \quad (1)$$

Here, the extrapolated value of the resistance, R_0, at 0 °C was 1.6361 Ω and the thermal coefficient of resistivity for the heater was $\theta = 0.002316$ Ω/°C.

In order to calculate the temperature of the microheater, the resistance variation with time was first determined. With the measured voltage drop of the precision resistors, $\Delta V_{PR}(t)$, and the resistance of the shunt-wound precision resistors, $R_{PR} = 2.5$ Ω, the current variation in the circuit was defined as

$$I(t) = \frac{\Delta V_{PR}(t)}{R_{PR}} \quad (2)$$

Then, with the measured voltage drop of the microheater, $\Delta V_{heater}(t)$, and the current calculated from Eq. (2), the variation of the resistance of the microheater could be represented as

$$R_{heater}(t) = \frac{\Delta V_{heater}(t)}{I(t)} \quad (3)$$

Finally, substituting the results from Eqs. (2) and (3) into Eq. (1), the temperature of the microheater could be obtained as

$$T_{heater}(t) = \frac{R_{PR} \cdot \frac{\Delta V_{heater}(t)}{\Delta V_{PR}(t)} - R_0}{\theta \cdot R_0} \quad (4)$$

In Eq. (4), R_{PR} , R_0 and θ are all known and $\Delta V_{PR}(t)$ and $\Delta V_{heater}(t)$ are obtained experimentally.

Power dissipation in the heater was also of interest in this investigation, not only for industrial applications, but also for the numerical simulation of the heat transfer in the microheater. Here, the power dissipation in the microheater can be determined as

$$\dot{Q}_{heater}(t) = I^2(t) \cdot R_{heater}(t) \quad (5)$$

However, Eq. (5) gives the total power dissipation in the microheater specimen, which includes two electrical wires soldered on the gold pads, the two gold pads themselves, and the platinum heater. In order to correctly calculate the power dissipated in the platinum heater alone, the following correction was applied

$$\dot{Q}_{Pt}(t) = \dot{Q}_{heater}(t)\frac{R_{Pt}}{R_{heater}}, \quad (6)$$

where $R_{Pt} = R_{heater} - R_{connection}$. It is important to note here that the resistance of the gold pads did not change significantly, since the resistance of the gold pads is small, the power density in the gold pad is very low, and the temperature of the gold pad was held relatively constant as indicated by a detailed 3D heat conduction analysis. Hence, if the connection resistance variation with temperature is neglected, $R_{connection} = 2 \times R_{wire} + 2 \times R_{Au} = 2 \times 0.1941 + 2 \times 0.3453 = 1.0788$ Ω, and the power consumed in the platinum heater can be determined. Similarly, the power consumed in the gold pad can also be calculated.

4. Experimental results and discussion

As discussed in the introductory section, the primary focus of the current investigation was to achieve the lowest nucleation temperature on a smooth platinum microheater, in water with or without dissolved gases, by controlling the power input (actually the overall voltage input). Here, the violent explosive boiling that results under more intense pulsed heating or higher power input is not discussed in detail, as the focus is on the boiling incipience on the microheater. This phenomenon is similar to that observed for low power heating, except that more small nucleate bubbles are generated and the final stable bubble diameter under higher power heating is much larger than what is typically generated under low power heating as observed in experiments. Additional related information can be found in [21,22].

In the following, the visualization of the bubble nucleation and bubble growth is first examined for quasi steady-state and pulsed heating, respectively. Then, the temperature variation and power dissipation

corresponding to the boiling phenomena are determined, illustrated and discussed. Finally, the bubble dynamics as resolved from the high-speed recording of the bubble growth is analyzed.

4.1. Visualization of microscale bubble nucleation and incipience temperature

4.1.1. Quasi steady-state boiling

In order to evaluate the difference between conventional boiling and boiling on a smooth surface, a sample with a small amount of residual defects from the metal sputtering process was selected. This test article had several cavities, approximately 5 μm in diameter. The bubble cavitation and growth process for this test article are shown in Fig. 5. It is obvious here that the bubble grows from the cavity and increases in size steadily and continuously because of the heated layer of liquid, which becomes thicker with time, due to the heat transfer from the microheater to the liquid. Thus, according to Hsu's model, the heat and mass transfer from the liquid to the vapor phase promotes bubble growth. This mechanism is also the driving mechanism in conventional boiling.

Fig. 6 illustrates bubble nucleation and growth on the smooth surface in the presence of dissolved gases. Here it can be seen that at the initial moment of bubble nucleation (0.004 s), a dramatic increase in the rate of bubble growth is observed, which is totally different from the bubble cavitation occurring in a cavity. This unique phenomenon provides definitive proof of the heterogeneous nucleation theory and explosive boiling, even under very slow heating rates.

Fig. 7 illustrates bubble nucleation and growth on a smooth surface immersed in water in which the dissolved gas has been removed by boiling for more than 30 min.

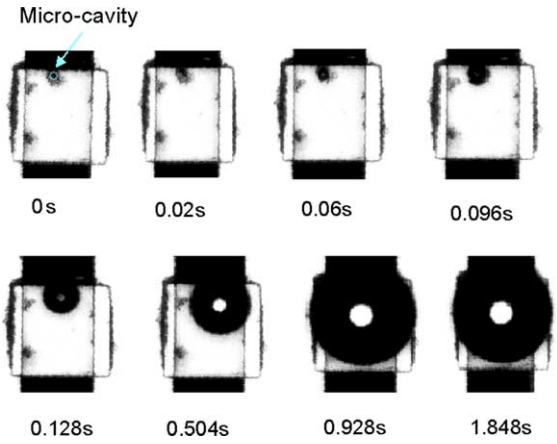

Fig. 5. Boiling incipience and bubble dynamics in water with gas dissolved for the quasi-steady state process from a microcavity with a diameter of 5 μm.

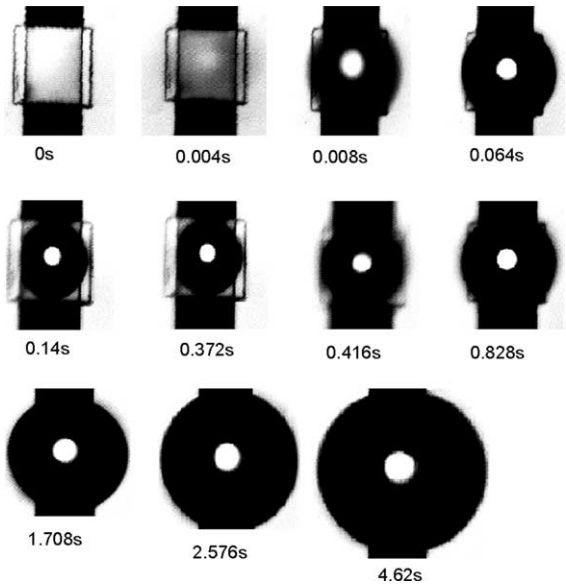

Fig. 6. Boiling incipience and bubble dynamics in water with gas dissolved for the quasi-steady state process on a smooth surface under 0.088 W power inputted.

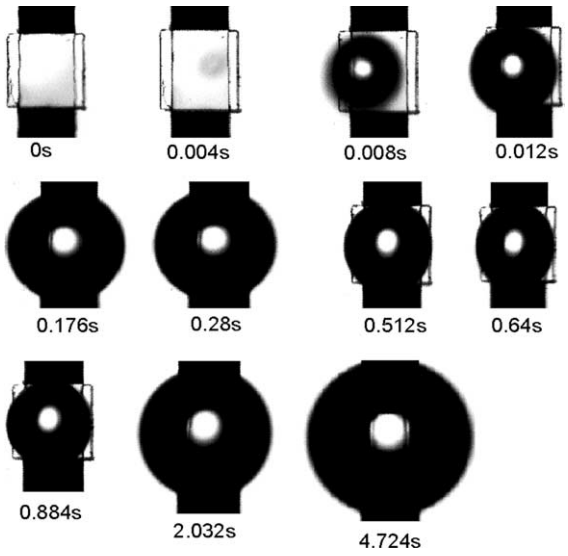

Fig. 7. Boiling incipience and bubble dynamics in degassed water for the quasi-steady state process on a smooth surface under 0.127 W power inputted.

Comparison of the phenomena in degassed water with those of the gas-dissolved water reveals the following: (1) the overall voltage input (or power input) for bubble generation in degassed water was much higher than that in gas-dissolved water; (2) the bubble size was smaller than the gas bubble due to the surface tension difference and the difference in the thermodynamic properties of

the gas and vapor; and (3) several small bubbles adjacent to a large bubble were nucleated spontaneously in the degassed water, as shown in Fig. 7 (0.004 s–0.012 s), due to the much higher surface temperature of the microheater. It is hypothesized here that the single large bubble observed in the experiments, shown in Figs. 6 and 7, results from the merging of many small bubbles generated in the central area of the heater in accordance with published experimental results and the kinetics of boiling, which yields large nucleation rates for a given superheat [6,7].

It should be noted that a common phenomenon observed during bubble evolution in both gas-dissolved and degassed water was that following the first stage of growth, the bubbles began to shrink slightly, and then grew steadily and approached an extremum that varied in accordance with the different voltage inputs.

The measured and computed temperature variations corresponding to Figs. 5–7 are shown in Fig. 8 with the power consumed in the microheater specimen indicated. As illustrated for boiling from a microcavity with an equivalent diameter of 5 μm, the boiling incipience temperature with gas dissolved in water was approximately 85 °C (Curve 3). This indicates approximately 15 °C of subcooling and agrees well with the theoretical analysis performed previously utilizing classical bubble survival theory [23]. This result demonstrates the accuracy of the present measurements and correlates quite well with the classical theoretical analysis for boiling incipience from a cavity. For bubble nucleation from a smooth surface, the temperature variations after boiling are also illustrated in Fig. 8, where Curve 1 is for degassed water and Curve 2 is for gas-dissolved water. For the gas-dissolved water, the measured incipience temperature was approximately 135 °C, and for degassed water this value approached 180 °C. Using the

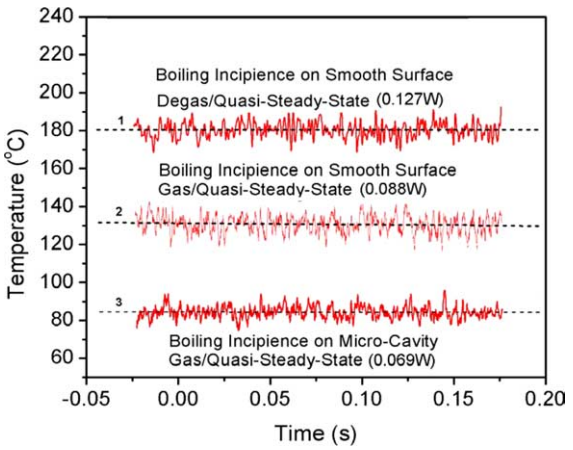

Fig. 8. Temperature variation after boiling incipience for quasi-steady state process (the data in the parenthesis is the power consumed on the microheater article).

3D steady-state heat conduction model described in detail in the Appendix, the temperature distribution in the microheater and on the surface can be resolved.

The numerical results obtained for the temperature distribution on the heater surface are shown in Figs. 9 and 10 for gas-dissolved water and for degassed water respectively. It can be seen here that for these two cases, the highest temperature in the central area of the heater was higher than the average bulk temperatures of the heater: 154 °C compared to 135 °C for gas-dissolved water and 205 °C compared to 180 °C for degassed water. Nevertheless, the observed explosive boiling is initiated in the central area of the heater and the bubble assumes an elliptical shape, which agrees well with the numerical results of the temperature distribution on the heater surface.

The predicted values for bubble nucleation are 230 °C for saturated gas-dissolved water and 265 °C for pure water from the theoretical analysis [23]. The possible reasons for the difference between the measured and predicted values are: (i) any unexpected impurities can decrease the incipience temperature and (ii) any unpredictable sub-micron defects on the heating surface can decrease the incipience temperature.

4.1.2. Pulsed heating boiling

Fig. 11 illustrates bubble nucleation and growth on the smooth surface with gas-dissolved water under a 120 ms pulse heating. Here it can be seen that, much like the quasi steady-state boiling case, a very large rate of bubble growth was obtained at the initial moment of bubble nucleation (0.004 s). Since considerable research has already been performed in the range of micro to millisecond pulses [3,4,7–12], a large pulse duration of 120 ms was utilized in the current study (this was also helpful due to the limited capture speed of the CCD camera) and for comparison with quasi steady-state phenomena.

Fig. 12 illustrates bubble nucleation and growth on a smooth surface with degassed water under a 120 ms pulse heating. Comparison of the resulting phenomena in degassed water with those occurring in the gas-dissolved water indicates the following: (1) the voltage amplitude of the pulse (or power input) for bubble generation in degassed water was much higher than that for the gas-dissolved water and (2) the speed of bubble collapse in the degassed water was faster due to the difference in surface tension and the difference in the thermodynamic properties of the gas and vapor. For both situations, the bubble collapses suddenly after the end of the pulse (This phenomenon was also observed by Deng et al. even for 1.6 ms pulsed heating [4]) due to the transient cooling of the ambient subcooled water (or mainly due to the transient cooling from the lower temperature gold pads with much higher thermal conductivity).

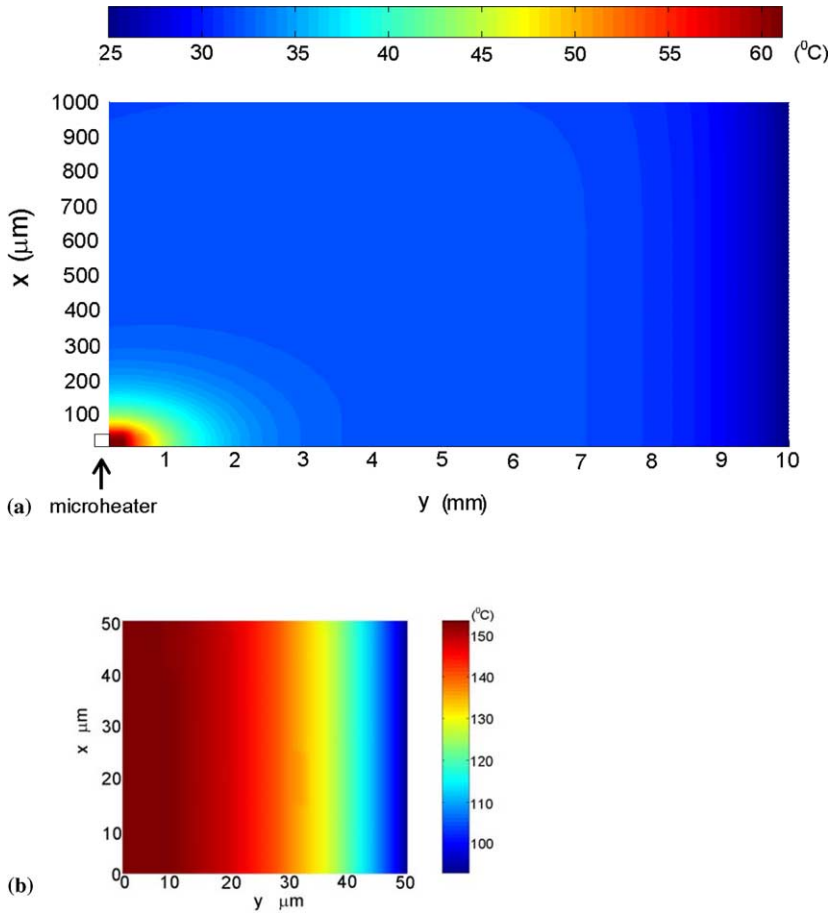

Fig. 9. Numerical simulation of the temperature distribution on the top surface of the microheater and gold pad for 0.085 W total power input-the averaged bulk temperature of microheater is 135 °C and the highest temperature on the platinum surface is 154 °C: (a) temperature distribution on the top surface of gold pad (the square indicates one fourth of the platinum microheater) and (b) temperature distribution on the top surface of the platinum microheater.

The measured temperature variations corresponding to Figs. 11 and 12 are shown in Figs. 13 and 14. It should be noted here that because there was no current in the circuit before and after the electrical pulse, there is no measurement of the temperature before or after the pulse. In Figs. 13(a) and 14(a), Curve 1 illustrates the measured temperature variations during 120 ms of pulsed heating. Curve 2 represents the numerical results of the bulk temperature of the platinum heater using a 3D unsteady-state heat conduction model with the measured power input, as shown in Figs. 13(b) and 14(b). The approach to calculating the power dissipated in the platinum heater and gold pads has been described previously. The detailed numerical model is also presented in the Appendix. The arrows in Figs. 13(a) and 14(a) identify the moment of boiling incipience as determined by the CCD camera. There are several reasons for the differences between Curve 1 and Curve 2 in Fig. 13(a) and 14(a). The principal one, however is that the measurement circuit utilized is not capable of measuring the voltage variation correctly at both edges of the pulse, due to the absence of current in the circuit. This needs to be improved in order to trace the variation of resistance at the edges of the pulse. Additionally, there remains some residual thermal stress from the microfabrication process, which is restored during the pulsed heating. Finally, the ambient noise is not negligible and this and several other minor and unexpected factors cannot be incorporated into the numerical simulation.

Under the pulsed heating applied in this investigation, the measured incipience temperature for the gas-dissolved water was approximately 150 °C, as shown in Fig. 13(a); for the degassed water, the measured incipience temperature was approximately 190 °C, as shown in Fig. 14(a).

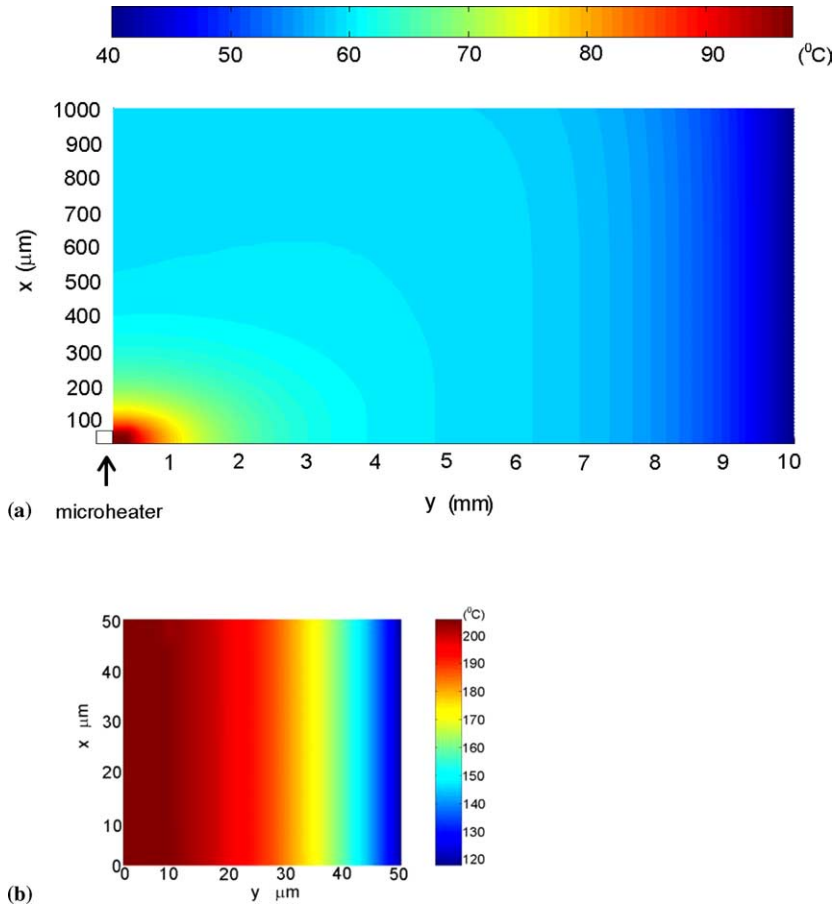

Fig. 10. Numerical simulation of the temperature distribution on the top surface of the microheater and gold pad for 0.117 W total power input-the averaged bulk temperature of microheater is 180 °C and the highest temperature on the platinum surface is 205 °C: (a) temperature distribution on the top surface of gold pad (the square indicates one fourth of the platinum microheater) and (b) temperature distribution on the top surface of the platinum microheater.

4.2. Bubble dynamics

Bubble dynamics examines the variation in bubble size with respect to time, the bubble interface velocity and the bubble interface acceleration. In the current investigation, bubble size evolution with time was resolved using the input from the high-speed camera. The equivalent radius of the bubble was measured by the camera software following calibration and correction for directional variations.

In order to accurately calculate the growth rate of a bubble, the following initial values are defined from the theory of kinetics,

$$r_0 = \frac{2\sigma}{[P_s(T_{Pt}) - P_{amb}]}, \tag{7}$$

$$\dot{r}_0 = 0, \tag{8}$$

where r_0 is the initial size of the bubble and $\dot{r}_0$ is the initial interface velocity of the bubble. The above definitions can be found in references that examine metastable liquids and homogeneous nucleation (e.g., Kagan [24]). If the highest temperature on the platinum surface, as determined from the numerical simulation, is used to determine the initial vapor pressure inside the bubble, r_0 will be a very small value, about ten nanometers. Thus, r_0 can be neglected and assumed to be zero $r_0 = 0$ for convenience.

Calculation of the bubble interface velocity and acceleration is accomplished as follows:

$$\dot{r}(n \cdot \Delta t) = \frac{r(n \cdot \Delta t) - r((n-1) \cdot \Delta t)}{\Delta t}$$

for the interface velocity (9)

$$\ddot{r}(n \cdot \Delta t) = \frac{\dot{r}(n \cdot \Delta t) - \dot{r}((n-1) \cdot \Delta t)}{\Delta t}$$

for the interface acceleration (10)

Here $n = 1, 2, \ldots$ and $\Delta t = 0.004$ s. Using Eqs. (9) and (10), the interface velocity, $\dot{r}(t)$, and acceleration of the

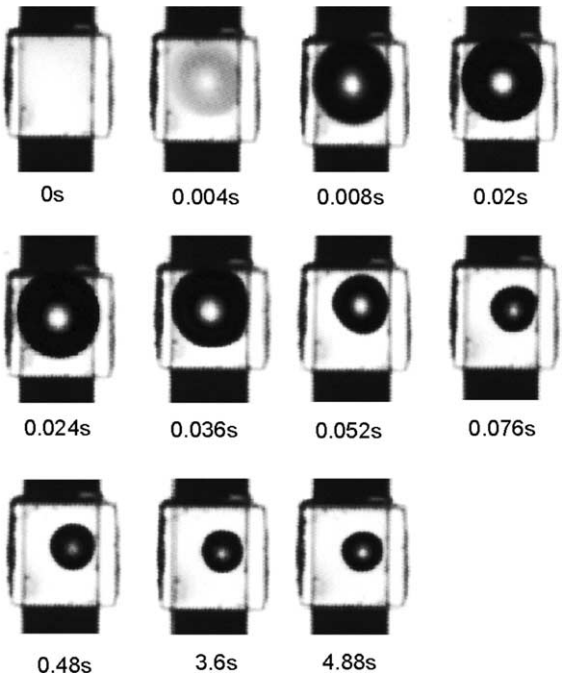

Fig. 11. Boiling incipience and bubble dynamics in water with gas dissolved for the pulsed-heating process on a smooth surface under 0.142 W power inputted.

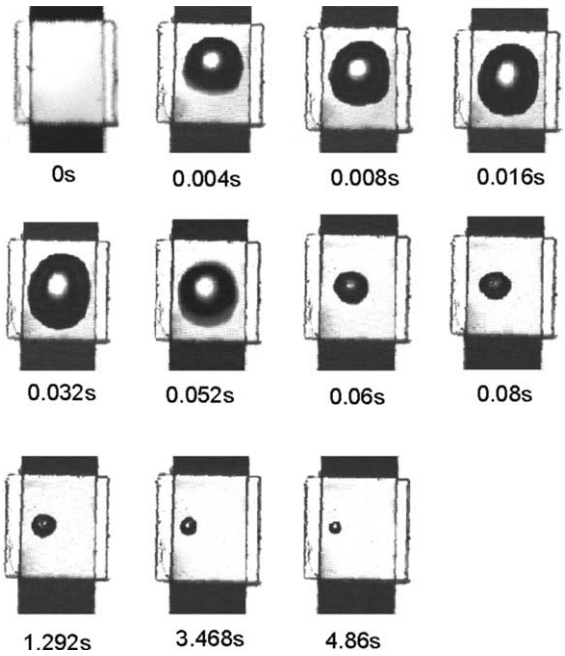

Fig. 12. Boiling incipience and bubble dynamics in degassed water for the pulsed-heating process on a smooth surface under 0.181 W power inputted.

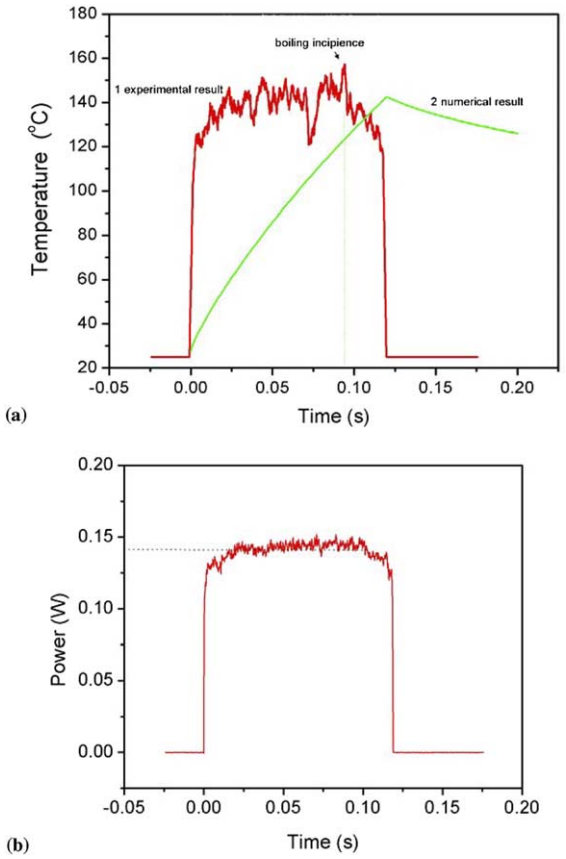

Fig. 13. Temperature and power variation of transient process with gas dissolved in water during pulsed heating: (a) temperature variation under pulsed heating (120 ms pulse) and (b) calculated power variation on the specimen (averaged value is 0.142 W).

bubble, $\ddot{r}(t)$, can be determined. Because of the time involved in analyzing and resolving every frame of the CCD movie, only the most typical and meaningful pictures were selected for use in the calculations.

4.3. Quasi steady-state

In Fig. 15, the bubble evolution with time, as illustrated in Figs. 5–7 is shown, are shown for a bubble initiating from a microcavity, a bubble from a smooth surface in water with gas dissolved, and a bubble from a smooth surface in degassed water, respectively. Fig. 15 clearly indicates, very clearly illustrates that the boiling from a microcavity is primarily controlled by the heat transfer, and that the variation of the bubble size was smooth and steady. However, for boiling from the smooth surface, there existed an obvious stage controlled by nonequilibrium pressure between the gas phase and the ambient phase. For the bubble from gas-dissolved water on a smooth surface, this dynami-

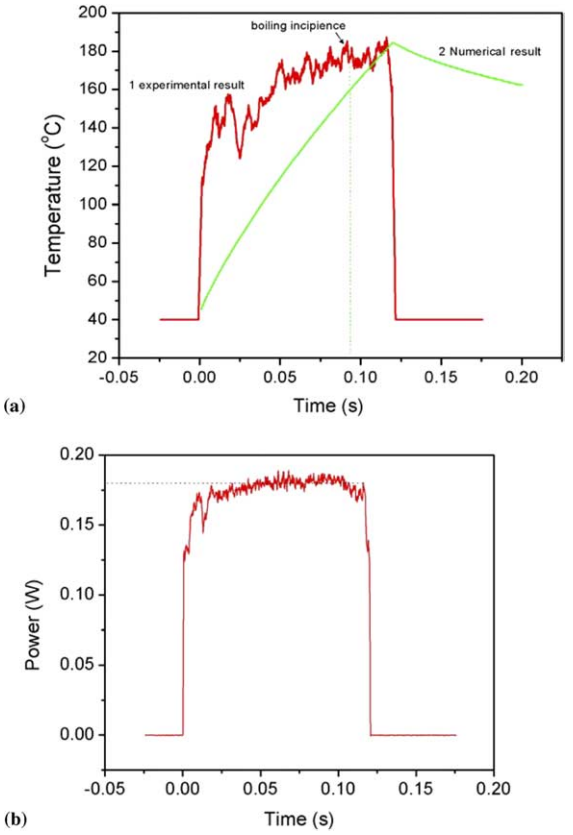

Fig. 14. Temperature and power variation of transient process for degassed water during pulsed heating: (a) temperature variation under pulsed heating (120 ms pulse) and (b) calculated power variation on the specimen (averaged value is 0.181 W).

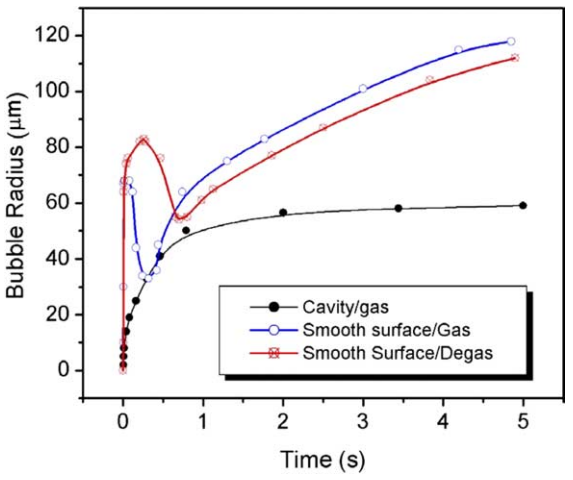

Fig. 15. Comparison #1 of bubble dynamics for quasi-steady state process as shown in Figs. 5–7—*Bubble growth and collapse*.

cally controlled stage lasted for 0.5 s, while for the bubble from degassed water, this stage lasted for 1.0 s. After this dynamically controlled stage, the bubble growth was similar to conventional boiling from a cavity. The reason for the different behavior for the current cases is that the input power for boiling on a smooth surface is much higher than for boiling from a cavity and the heated liquid layer is much thicker than when there is a lower power input.

The difference between the bubble from gas-dissolved water on a smooth surface and the bubble from degassed water on a smooth surface is that the extremum of the vapor bubble size is smaller than for the gas bubble, even if the input power for the vapor bubble generation is higher than that for gas bubble generation. The reason for this difference is that the surface tension with gas dissolved water was reduced slightly and the noncondensible gases behaved much differently from the vapor under similar heating conditions i.e., each of these follows the thermodynamic equation of state for the particular case.

The interface velocities and accelerations from Fig. 15 as computed using Eqs. (9) and (10) are shown in Fig. 16 for three different situations for the quasi steady-state heating process. Fig. 16 reveals that the bubble dynamics associated with explosive boiling is much different from conventional boiling from a cavity. The initial acceleration of the explosive boiling is much higher than for bubbles from cavities. The initial acceleration for the explosive boiling is on the order of 10 m/s^2 if the data are extrapolated as $t \to 0$. Once more, because of the influence of the noncondensible dissolved gas, the initial velocity and acceleration of a gas bubble were higher than for a vapor bubble.

4.3.1. Pulsed heating

Fig. 17 illustrates the bubble evolution under pulsed heating with respect to time as depicted in Figs. 11 and 12 for bubbles emanating on a smooth surface from gas-dissolved water and degassed water, respectively. From a comparison of Figs. 17(a) and 15, the difference between the quasi steady-state and pulsed heating is obvious. There exists a sudden intermediate shrinking of bubble size which takes place near the end of the pulse, but it is different from the shrinking phenomena observed in quasi steady-state heating. In quasi steady-state heating, the intermediate shrinking phenomenon reflects the dynamic control stage of bubble growth, mainly due to the variation of pressure inside the bubble. In the pulsed heating case, this intermediate shrinking results from the combination of the cooling of the subcooled water around the bubble (which is different from the quasi steady-state heating) and the variation of the pressure inside the bubble. Fig. 17(b) is a semi-log and semi-normal replotting of Fig. 17(a). Here it is clear that the end of the pulse has a significant influence

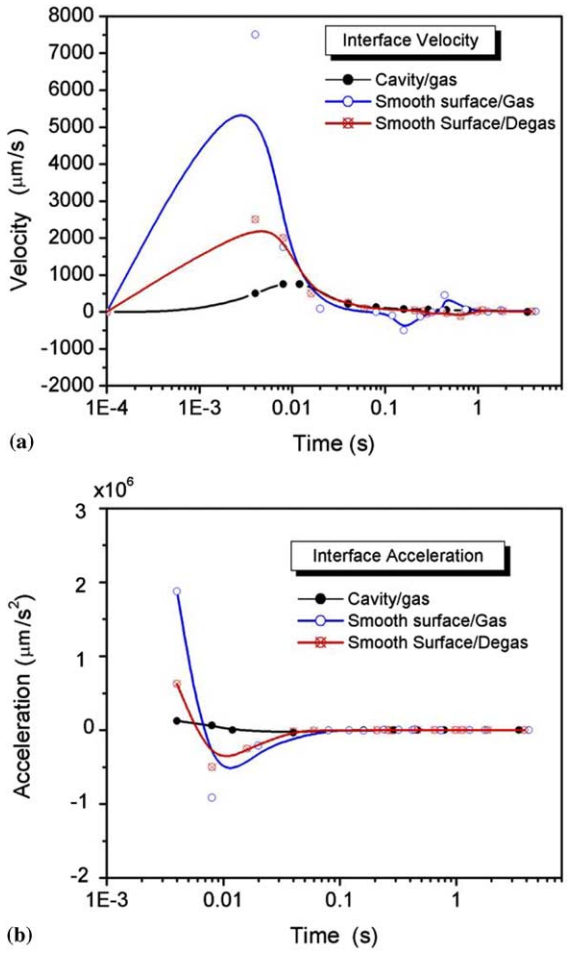

Fig. 16. Comparison #2 of bubble dynamics for quasi-steady state process as shown in Figs. 5–7—*Interface velocity and acceleration*: (a) interface velocity of nucleated bubble and (b) interface acceleration of nucleated bubble.

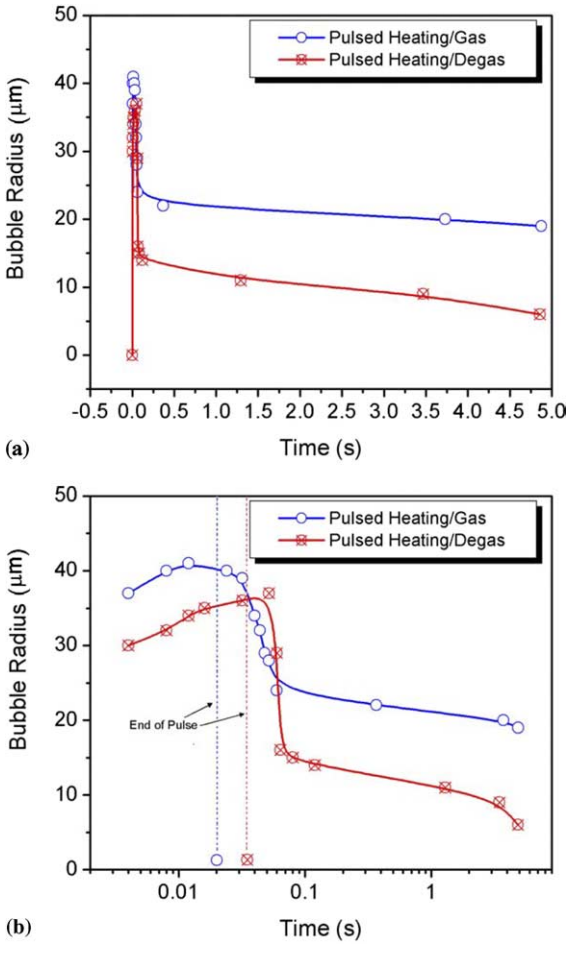

Fig. 17. Comparison #1 of bubble dynamics for pulsed heating process as shown in Figs. 11 and 12—*Bubble growth and collapse*: (a) normal coordinate and (b) semi-log coordinate.

on the bubble shrinking phenomenon and that this sudden decrease in bubble size is much larger for a bubble in degassed water than for a bubble in gas-dissolved water, due to the effects of the noncondensible gas, which delays the bubble size reduction.

The computed interface velocities and accelerations obtained from Fig. 17 using Eqs. (9) and (10) are shown in Fig. 18 for gas-dissolved water and degassed water under pulsed heating. In Fig. 18, the initial acceleration of the explosive boiling is on the order of 100 m/s^2 if we extrapolate the curve to $t \to 0$ for this 120 ms pulsed heating. Because, in this study, the duration of the heating pulse was comparatively large and because the measured gradients of the temperature variations of the platinum heater during the pulsed heating, as shown in Figs. 13(a) and 14(a), were not large, the measured interface velocity and accelerations were not much higher than the measured values for quasi steady-state, as illustrated by comparing Figs. 16 and 18. In some previous experimental studies (e.g., in references [8,9]), a measured velocity on the order of 10 m/s and an acceleration on the order of 10^7 m/s^2 were obtained using a heating pulse on the order of microseconds. By comparison, here it is clear that transient heating will substantially increase the violence of the explosive boiling.

4.4. Marangoni flow

During this study the authors encountered an interesting phenomenon. For quasi steady-state heating in a degassed liquid, slight reductions in the input power after the bubble had reached its extremum, resulted in decreases in the bubble size, and if the bubble size (or the vapor–liquid interface contact line on the heater surface) had not reached a point that extended beyond the

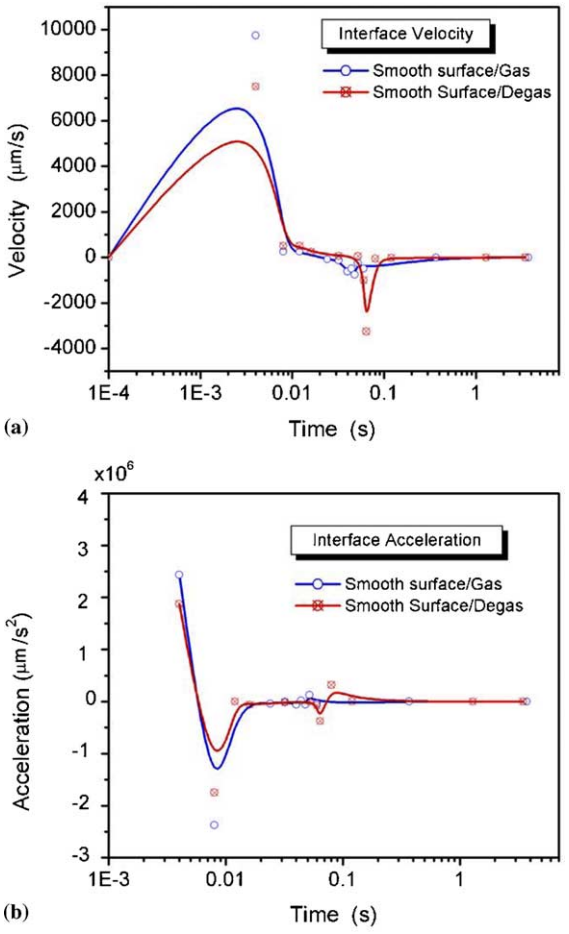

Fig. 18. Comparison #2 of bubble dynamics for pulsed heating process as shown in Figs. 11 and 12—*Interface velocity and acceleration*: (a) interface velocity of nucleated bubble and (b) interface acceleration of nucleated bubble.

heater surface (refer to Fig. 19), the Marangoni phenomenon was induced by the temperature gradient between the heater and the ambient subcooled water and could be observed on the interface. When this occurred, it appeared that some kind of unstable fluid flow was initiated at the vapor–liquid interface, which took the form of tiny clusters (or drops) moving randomly. This phenomenon is different from the observation reported by Kim et al. [13] and no previous reports of experimental studies in which this interface instability induced by the Marangoni flow have been observed, have been reported.

5. Conclusions

The current study utilized microfabrication techniques to obtain quantitative results for explosive boiling occurring on smooth surfaces, i.e., heterogeneous nucleation, as a function of the nucleation or boiling incipience temperature. The behavior and dynamics of the bubble along with the influence of the noncondensible dissolved gas on the incipience temperature and bubble dynamics are reported and discussed. The results indicate that for a smooth surface, i.e., a roughness equal to the critical bubble size and homogeneous nucleation, explosive boiling is the dominant boiling mode no matter how slowly the heating rate. This observation alone represents substantial evidence and support for the classical kinetics of boiling. In addition, the boiling incipience and bubble behavior from a smooth surface were observed to be much different than for the boiling taking place on a rough surface, even when the size of the nucleation cavity is in the range of microns, which represents the more conventional boiling phenomena, which can be explained by Hsu's proposed theory of bubble survival.

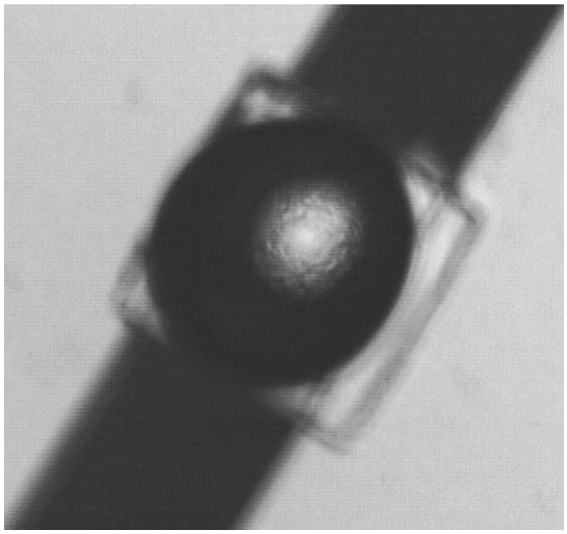

Fig. 19. Marangoni flow at the bubble interface induced by the surface tension gradient because of the temperature gradient in the heated microlayer of water.

Bubble growth from a smooth surface was found to have a dynamic stage, the duration of which depends on the transient process i.e., the heating rate and pulse duration, the properties of the liquid i.e., degassed or gas dissolved, and the degree of subcooling present. Further, the noncondensible dissolved gas was found to have a significant effect on the boiling incipience and bubble behavior, resulting in a decrease in the nucleation temperature, but an increase in the degree of violence associated with the explosive boiling, and may significantly postpone bubble collapse during transient heating. This later effect is of value in MEMS and other industrial applications.

Based upon the experimental evidence presented here, it is clear that kinetic theory can be used to explain boiling incipience in principle and can serve as a guide for the design of the microscale heat transfer devices used in MEMS applications.

Acknowledgements

The authors would like to acknowledge the support of the Office of Naval Research Grant number ONR N140010454 and the National Science Foundation, Grant number CTS-0312848.

Appendix A

The numerical model used in this investigation is presented here in detail. Because of the axisymmetric configuration of the platinum heater, the numerical domains consist of only one fourth of the heater and one half of the gold pad on one side, as shown in Fig. 20. For the quasi steady-state heating process, a coupled 3D steady-state heat conduction model was used, which resulted in a governing equation of the form

$$\frac{\partial}{\partial x}\left(\lambda_i \frac{\partial T}{\partial x}\right)+\frac{\partial}{\partial y}\left(\lambda_i \frac{\partial T}{\partial y}\right)+\frac{\partial}{\partial z}\left(\lambda_i \frac{\partial T}{\partial z}\right)+\dot{Q}_i=0 \quad \text{(A.1)}$$

i denotes platinum and gold respectively. This equation is subject to the following thermal boundary conditions (refer to Fig. 20):

$$x_1=0 \quad \text{and} \quad x_2=0, \quad -\lambda_i \frac{\partial T}{\partial x}=0, \quad \text{(A.2a)}$$

$$x_1=50\ \mu\text{m} \quad \text{and} \quad x_2=1000\ \mu\text{m},$$

$$-\lambda_i \frac{\partial T}{\partial x}=\alpha(T-T_0)+\varepsilon_i \sigma T^4, \quad \text{(A.2b)}$$

$$y_1=0, \quad -\lambda_{\text{Pt}} \frac{\partial T_{\text{Pt}}}{\partial y}=0, \quad \text{(A.2c)}$$

$$y_1=50\ \mu\text{m}, \quad \text{and} \quad y_2=0 \quad \text{if } x_2 \quad \text{and}$$

$$z_2 \in \text{connection area}, \quad -\lambda_{\text{Pt}} \frac{\partial T_{\text{Pt}}}{\partial y}=-\lambda_{\text{Au}} \frac{\partial T_{\text{Au}}}{\partial y}, \quad \text{and}$$

$$y_2=0 \quad \text{if } x_2 \quad \text{and} \quad z_2 \notin \text{connection area},$$

$$-\lambda_{\text{Au}} \frac{\partial T}{\partial y}=\alpha(T-T_0)+\varepsilon_{\text{Au}} \sigma T^4, \quad \text{(A.2d)}$$

$$y_2=10{,}000\ \mu\text{m}, \quad T_{\text{Au}}=T_0, \quad \text{(A.2e)}$$

$$z_1=0 \quad \text{and} \quad z_2=0, \quad -\lambda_i \frac{\partial T}{\partial z}=0, \quad \text{(A.2f)}$$

$$z_1=0.17\ \mu\text{m} \quad \text{and} \quad z_2=0.32\ \mu\text{m},$$

$$-\lambda_i \frac{\partial T}{\partial z}=\alpha(T-T_0)+\varepsilon_i \sigma T^4, \quad \text{(A.2g)}$$

where Eqs. (A.2b) and (A.2g) yield the third boundary condition. Eqs. (A.2a), (A.2c) and (A.2f) assume adiabatic boundary conditions, because of the symmetric configuration of the platinum heater and the very low conductivity of the substrate glass. Eq. (A.2d) assumes a constant heat flux at the connection between the platinum heater and the gold pad. The properties of the materials considered here are shown in Table 1. It should be noted here that in Eq. (A.1) $\dot{Q}$ can be calcu-

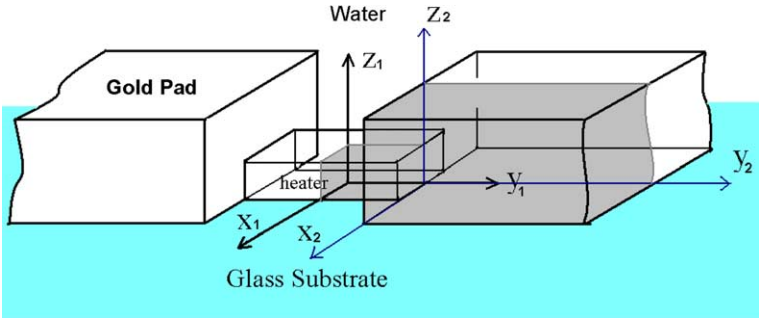

Fig. 20. Numerical domain (gray area) of 3D heat conduction in microheater specimen (not in scale).

Table 1
Properties of materials in interest

	ε	e_R (Ω m)	TCR (ppm/°C)	λ (W/m °C)	C_P (J/kg °C)	ρ (kg/m^3)
Platinum	0.03	1.06×10^{-7}	3850	71.4	133	21460
Gold	0.02	2.21×10^{-8}	4000	310.0	128	19280
Water	–	–	–	0.6	4188	980
Pyrex glass	–	–	–	1.4	740	2190

lated from Eqs. (5) and (6) and divided by the volume of platinum or gold pad respectively.

In the boundary conditions given in Eqs. (A.2b) and (A.2g), the natural convection heat transfer coefficient is adopted from the well-accepted correlation [25] for fluid natural convection on a horizontal heated surface

$$Nu = 0.54Ra_{\mathrm{L}}^{0.25} \quad 10^5 < Ra_{\mathrm{L}} < 2\times 10^7 \quad \text{and}$$
$$Pr > 0.5 \text{ for a liquid} \tag{A.3}$$

Here Ra_{L} is the Raleigh number $Ra_{\mathrm{L}} = Gr_{\mathrm{L}} \cdot Pr$ and Gr_{L} is the Grashof Number,

$$Gr_{\mathrm{L}} = \frac{\beta \cdot \Delta T \cdot g \cdot (L)^3}{v_l^2} \tag{A.4}$$

L is the characteristic length of the square plate, $\beta = 1/T$, $g = 9.8$ and $\Delta T = T - T_0$. In the expressions given for the boundary conditions, Eqs. (A.2b) and (A.2g), ε is the emissivity of a gray body and here, for the platinum surface $\varepsilon \approx 0.03$ and for gold $\varepsilon \approx 0.02$ for a large range of temperature [26], and σ is the Stefan–Boltzmann constant $\sigma = 5.669\times 10^{-8}$ W/m^2 K^4.

The transient heat conduction can be simulated using a 3D unsteady-state heat conduction model which yields the following governing equation:

$$\rho_i C_{P_i} \frac{\partial T}{\partial t} = \frac{\partial}{\partial x}\left(\lambda_i \frac{\partial T}{\partial x}\right) + \frac{\partial}{\partial y}\left(\lambda_i \frac{\partial T}{\partial y}\right) + \frac{\partial}{\partial z}\left(\lambda_i \frac{\partial T}{\partial z}\right) + \dot{Q}_i(t) \tag{A.5}$$

with the same boundary conditions used in Eqs. (A.2a)–(A.2g) and subjected to the following initial conditions:

$$T(0,x) = T_0 \tag{A.6}$$
$$\dot{Q}_i(t) = \dot{Q}_i \cdot \lfloor h(t) - h(t - t_{\mathrm{p}}) \rfloor, \tag{A.7}$$

where $\dot{Q}$ represents the power intensity of the pulse and t_{P} is the time duration of the pulse. Note that the quantity $h(t)$ in Eq. (A.7) is the unit-step function defined by

$$h(t) = \begin{cases} 0 & \text{for} \quad t < 0 \\ 1 & \text{for} \quad t \geqslant 0 \end{cases} \tag{A.8}$$

For steady-state conduction, Eq. (A.1), a line-by-line interaction and a tri-diagonal matrix algorithm (TDMA) method with a Thomas algorithm and successive under-relaxation iterative methods were used to obtain the 3D temperature distribution, $T(x,y,z)$. The convergence criterion was chosen as $\sum\sum\sum |T(i,j,k) - T_0(i,j,k)| \leqslant 10^{-2}$ and the total grid number N was 10,625 $(i(x_1)\times j(y_1)\times k(z_1) 25\times 25\times 17)$ for domain 1, the platinum heater, and 160,000 $(i(x_2)\times j(y_2)\times k(z_2) 100\times 50\times 32)$ for domain 2, the gold pad. The above criterion for the mean square root error (MSRE) of $|T(i,j,k) - T_0(i,j,k)| \approx \frac{\sum\sum\sum\sqrt{(T(i,j,k)-T_0(i,j,k))^2}}{N} \leqslant 1\times 10^{-6}$ was utilized.

For unsteady-state conduction, a semi-implicit method along the z-direction with the Thomas algorithm was used to solve the time-resolved temperature $T(t,x,y,z)$.

References

[1] I. Mudawar, Assessment of high-heat-flux thermal management schemes, IEEE Trans. Comp. Packag. Technol. 24 (2) (2001) 122–141.

[2] H. Yuan, H.N. Oğuz, A. Prosperetti, Growth and collapse of a vapor bubble in a small tube, Int. J. Heat Mass Transfer 42 (1999) 3643–3657.

[3] J. Tsai, L. Lin, Active microfluidic mixer and gas bubble filter driven by thermal bubble micropump, Sens. Actuator, A 97–98 (2002) 665–671.

[4] P. Deng, Yi-Kuen Lee, P. Cheng, The growth and collapse of a microbubble under pulse heating, Int. J. Heat Mass Transfer 46 (2003) 4041–4050.

[5] Y. Hsu, On the size range of active nucleation cavities on a heating surface, ASME J. Heat Transfer 84 (1962) 207–216.

[6] R. Cole, Boiling nucleation, Advances in Heat Transfer, vol. 10, Academic Press, Inc., 1974, pp. 86–166.

[7] V.P. Skripov, Metastable Liquids, John Wiley & Sons, New York, 1974.

[8] Y. Iida, K. Okuyama, K. Sakurai, Boiling nucleation on a very small film heater subjected to extremely rapid heating, Int. J. Heat Mass Transfer 37 (17) (1994) 2771–2780.

[9] Z. Zhao, S. Gold, D. Poulikakos, Pressure and power generation during explosive vaporization on a thin-film microheater, Int. J. Heat Mass Transfer 43 (2000) 281–296.

[10] O.C. Thomas, R.E. Cavicci, M.J. Tarlov, Effect of surface wettability on fast transient microboiling behavior, Langmuir 19 (2003) 6168–6177.

[11] C.T. Avedisian, W.S. Osborne, F.D. McLeod, and C.M. Curley, Measuring bubble nucleation temperature on the surface of a rapidly heated thermal ink-jet heater immersed in a pool of water, in: Proceedings of the Royal Society of London Series A- Mathematical Physical and Engineering Sciences 455(1991) (1999) pp. 3875–3899.

[12] Z. Yin, A. Prosperetti, J. Kim, Bubble growth on an impulsively powered microheater, Int. J. Heat Mass Transfer 47 (2004) 1053–1067.

[13] J. Kim, J.F. Benton, D. Wisniewski, Pool boiling heat transfer on small heaters: effect of gravity and subcooling, Int. J. Heat Mass Transfer 45 (19) (2002) 3919–3932.

[14] T. Chen, J.F. Klausner, J.N. Chung, Subcooled boiling heat transfer and dryout on a constant temperature microheater, Int. J. Heat Fluid Flow 25 (2) (2004) 274–287.

[15] H.C. Lee, B.D. Oh, S.W. Bae, M.H. Kim, J.Y. Lee, I.S.W. Song, Partial nucleate boiling on the microscale heater maintaining constant wall temperature, J. Nucl. Sci. Technol. 40 (10) (2003) 768–774.

[16] A. Prosperetti, M.S. Plesset, Vapour-bubble growth in a superheated liquid, J. Fluid Mech. 85 (part 2) (1978) 349–368.

[17] A. Asai, Bubble dynamics in boiling under high heat flux pulse heating, J. Heat Transfer 113 (1991) 973–979.

[18] H.S. Lee, H. Merte Jr., Spherical bubble growth in liquids in uniformly superheated liquids, Int. J. Heat Mass Transfer 39 (12) (1996) 2427–2447.
[19] D.L. Zeng, F. Wang, C. Liu, Bubble growth in superheated liquid based on nonequilibrium thermodynamic theory, Sci China Ser A 41 (1) (1998) 93–98.
[20] J. Li, G.P. Peterson, P. Cheng, Mechanical non-equilibrium consideration of homogeneous bubble nucleation for an unsteady-state boiling process, Int. J. Heat Mass Transfer 48 (15) (2005) 3081–3096.
[21] Y. Iida, K. Okuyama, T. Endou, N. Kanda, Boiling nucleation on a very small film heater subjected to extremely rapid heating—effect of ambient pressure on bubble formation by fluctuation nucleation, JSME Int. J. Ser. B—Fluids Thermal Eng. 40 (2) (1997) 250–256.
[22] J. Li, Z.F. Zhang, D.Y. Liu, Experimental and theoretical study on rapid transient nucleated boiling, Progr. Nat. Sci. 11 (7) (2001) 529–535.
[23] J. Li, P. Cheng, Bubble cavitation in a microchannel, Int. J. Heat Mass Transfer 47 (2004) 2689–2698.
[24] Y. Kagan, The kinetics of boiling of a pure liquid, Russ. J. Phys. Chem. 34 (1) (1960) 42–46.
[25] A.F. Mills, Heat Transfer, second ed., Prentice Hall, Upper Saddle River, 1999.
[26] J.P. Holman, Heat Transfer, fifth ed., McGraw-Hill, Inc. (Kogakusha, Ltd.), Tokyo, 1981.